INTERNATIONAL JOURNAL FOR NUMERICAL METHODS IN BIOMEDICAL ENGINEERING
Int. J. Numer. Meth. Biomed. Engng. 2013; **00**:1–14
Published online in Wiley InterScience (www.interscience.wiley.com). DOI: 10.1002/cnm

Development of Mapped Stress-Field Boundary Conditions Based on a Hill-Type Muscle Model

P. Cardiff[1]*, A. Karač[2], D. FitzPatrick[1], R. Flavin[1] and A. Ivanković[1]

[1]*University College Dublin, School of Mechanical and Materials Engineering, Belfield, D4, Dublin, Ireland*
[2]*University of Zenica, Faculty of Mechanical Engineering, Fakultetska 1, Zenica, Bosnia and Herzegovina*

SUMMARY

Forces generated in the muscles and tendons actuate the movement of the skeleton. Accurate estimation and application of these musculotendon forces in a continuum model is not a trivial matter. Frequently musculotendon attachments are approximated as point forces, however, accurate estimation of local mechanics requires a more realistic application of musculotendon forces. This paper describes the development of mapped Hill-type muscle models as boundary conditions for a finite volume model of the hip joint, where the calculated muscle fibres map continuously between attachment sites. The applied muscle forces are calculated using active Hill-type models, where input electromyography signals are determined from gait analysis. Realistic muscle attachment sites are determined directly from tomography images. The mapped muscle boundary conditions, implemented in a finite volume structural OpenFOAM solver, are employed to simulate the mid-stance phase of gait using a patient specific natural hip joint, and a comparison is performed with the standard point load muscle approach. It is concluded that physiological joint loading is not accurately represented by simplistic muscle point loading conditions; however, when contact pressures are of sole interest, simplifying assumptions with regard to muscular forces may be valid. Copyright © 2013 John Wiley & Sons, Ltd.

Received ...

KEY WORDS: active Hill muscle models; mapped muscle boundary conditions; Finite Volume method; OpenFOAM; electromyography; contact stress analysis

1. INTRODUCTION

Numerical analysis of the hip joint is increasingly being considered to help orthopaedists make confident surgical decisions, and due to the restrictions of *in vivo* and *in vitro* studies, these *in silico* studies have the capacity to provide an effective solution. Early models [1–3] of the pelvis and femur (thigh bone) were generated from 2-D radiograph images and employed point forces to approximate the joint loading generated by the articular contact and soft tissues. With growing computational resources, it has become possible to capture complex 3-D patient specific

*Correspondence to: University College Dublin, School of Mechanical and Materials Engineering, Belfield, D4, Dublin, Ireland. E-mail: philip.cardiff@ucd.ie

Copyright © 2013 John Wiley & Sons, Ltd.

joint geometry using tomographic techniques such as computed tomography (CT) and magnetic resonance imaging (MRI) [4–13], where contact procedures have been employed to resolve the articular traction distributions [7, 14]. Nevertheless, the intricate muscular loading experienced by the joint is still commonly represented using simplistic point load approaches. Many models do not explicitly include muscle forces, instead opting for implicit inclusion through application of a total joint force [7–9, 15–18]. Muscle forces, when explicitly included, are typically sourced from published hip joint loading data, although some authors have included time-varying muscle forces using basic passive Hill-type muscle models [9, 17–20]. Accounting for muscles using simplistic methods, such as *point loads*, has many advantages such as straightforward implementation and representation of many muscles with little cost, however, unrealistic local stress distributions are present at the muscle attachment sites resulting in erroneous local mechanics. Consequently, the true mechanics of the joint may not be captured correctly.

It is clear that hip joint models promise great potential, but may be limited by simplistic representations of musculotendon loading. Accordingly, the current research aims to develop mapped muscle models that realistically represent the complex physiological loading imposed by the periarticular muscles, where both the active and passive components of muscle force are captured using Hill-type muscle models.

2. METHODS

In this section, the employed Hill-type muscle models which approximate the musculotendon force are presented, including a description of the adopted force-length/force-velocity relationships, tendon model, and activation dynamics. Subsequently, the developed muscle mapping procedure is presented. Finally, a brief summary of the muscle attachment identification approach is given along with descriptions of the finite volume structural solver and solution procedure.

2.1. Hill-type Muscle Models

In this work a Hill-type muscle model consisting of three components [19,20], namely, a contractile element, a parallel elastic element and a series elastic element, is employed. The force generated in the contractile element depends on muscle activation, muscle length and muscle velocity, the parallel elastic element force depends on muscle length and muscle velocity, while the series elastic element force depend solely on muscle length. The magnitude of time-varying muscle force F_m predicted by the model is given in the general form by:

$$F_m = F_{max} \left(f_v f_{al} a_m + f_{pl} + f_d \right) \tag{1}$$

where F_{max} is the maximum isometric muscle force, f_v is the velocity-dependent active force scaling factor, f_{al} is the length-dependent active force scaling factor, a_m is the time varying muscle activation, f_{pl} is length-dependent passive force scaling factor and f_d is the muscle damping component.

Copyright © 2013 John Wiley & Sons, Ltd.

Prepared using cnmauth.cls
DOI: 10.1002/cnm

The employed force-velocity parameter, f_v, is described mathematically by:

$$f_v = \begin{cases} \dfrac{F_{max}b + av_m}{b - v_m} & , v_m \leq 0 \\ F_{ecc}^m F_{max} - (F_{ecc}^m - 1)\dfrac{F_{max}b^{'} - a^{'}v_m}{b^{'} + v_m} & , v_m > 0 \end{cases} \tag{2}$$

where v_m is the current muscle velocity; positive velocities correspond to concentric muscle motion (the muscle getting shorter), and negative velocities correspond to eccentric muscle motion (the muscle getting longer). The parameters a, $a^{'}$, b, $b^{'}$, and F_{ecc} are shape parameters given in Table I [19,21]. The maximum voluntary muscle contraction velocity v_{max} is assumed to be $10l_m^o\mathrm{s}^{-1}$ [19], and l_m^o is the optimal muscle fibre length – the length at which the maximum isometric force can be generated.

The active force-length scaling factor, f_{al}, originating from the overlap of proteins in the belly of the muscle [22], is represented by an empirically determined parabolic shape [23, 24], fit with natural cubic splines [25] as given in Figure 1.

The passive force-length scaling factor, f_{pl}, applies a resistive force when stretched beyond a resting length, and is represented as an exponential curve [21]:

$$f_{pl} = \begin{cases} \dfrac{e^{10(l_m - 1)}}{e^5} & , l_m \geq l_m^o \\ 0 & , l_m < l_m^o \end{cases} \tag{3}$$

Muscle damping is included as:

$$f_d = B_m v_m \tag{4}$$

where the muscle damping coefficient $B_m = 1\ \mathrm{Nsm}^{-1}$ [20,21] .

Muscle Activation The muscle activation required by the Hill-type models has been determined from EMG signals measured during gait analysis (walking speed of 1.4 $\mathrm{m/s}$). The signals are gathered using a surface electromyography (EMG) system where electrodes are adhered to the skin directly above the muscles of interest, using the CODA (Codamotion V6.69H-CX1/MPX30) movement analysis hardware and software [26, 27, 29, 30]. These muscle electrodes transmit real time signals to the CODA system via a wireless transmitter unit attached to the back of the subject.

The raw EMG signals are initially rectified, converting all negative amplitudes to positive amplitudes, and a low-pass second order 20 Hz Butterworth filter [31, 32] algorithm is applied to minimise the non-reproducible random nature of the signal, with minimial phase shift. The Matlab [33] zero-phase filter function, `filtfilt`, has been employed, with the coefficients generated using the `butter` function. Figure 2 compares an initial raw EMG signal with the final rectified, filtered and normalised signal, termed muscle excitation u_t. This muscle excitation signal is input into the muscle models, but there is a delay before the muscle becomes active; this connection between muscle excitation u_t and muscle activation a_t is governed by activation dynamics.

Activation dynamics, the process of transforming the muscle excitation signal u_m to muscle activation a_m, is approximated using the first-order differential relation [19,21,34]:

$$\frac{\partial a_m}{\partial t} = \frac{1}{\tau}\left(u_m - K_{act}a_m\right) \tag{5}$$

Copyright © 2013 John Wiley & Sons, Ltd.

Prepared using cnmauth.cls
DOI: 10.1002/cnm

where τ is activation time constant:

$$\tau = \begin{cases} \tau_{act} & , u_m > a_m \\ \dfrac{\tau_{act}}{\beta} & , u_m \leq a_m \end{cases} \tag{6}$$

with $\tau_{act} = 0.012$, $\beta = 0.5$ [34], and $K_{act} = 1$ [34].

Tendon Model The force-strain relationship for tendon is represented by the piece-wise function [19,21,34]:

$$T_t = \begin{cases} 0 & , \varepsilon_t \leq 0 \\ 1480.3\varepsilon_t^2 & , 0 < \varepsilon_t \leq 0.0127 \\ 37.5\varepsilon_t - 0.2375 & , \varepsilon_t \geq 0.0127 \end{cases} \tag{7}$$

where tendon strain ε_t is defined in terms of the tendon length, l_t, and the tendon slack length, l_t^s:

$$\varepsilon_t = \frac{l_t - l_t^s}{l_t^s} \tag{8}$$

The initial nonlinear *toe* region can be explained by tendon being composed of collagen that has a wave-like crimp, which gradually straightens out as the fibres take up load.

Hill-Type Model Governing Relations Many Hill-type muscle models assume the muscle to be massless *i.e.* the ability of the muscle to produce force is unaffected by its own mass. However, in the current study muscle mass is included, producing a more numerically stable model with reduced unphysical high frequency oscillations [35]. By employing Newton's second law, the governing Hill-type model relationship is derived:

$$F_t - F_m^{eff} = M_m \frac{\partial^2 l}{\partial t^2} \tag{9}$$

where the net force on the muscle mass, M_m, resulting in a net muscle mass acceleration, $\partial^2 l / \partial t^2$, is given by the difference between the tendon force, F_t, and the effective muscle force, F_m^{eff}, and l is the relative muscle position, related to the muscle length and tendon length.

The effective muscle force, F_m^{eff}, is less than the actual generated muscle force, F_m, as illustrated schematically in Figure 3, and described mathematically as:

$$F_m^{eff} = F_m \cos \alpha_m \tag{10}$$

where the muscle pennation angle, α_m, describes the angle at which the muscle fibres pull relative to the tendon fibres. Since pennation angle has been found to vary with changing muscle length, a dynamic muscle pennation angle, dependent on muscle length, is applied in the current model, given as [20,21]:

$$\alpha_m = sin^{-1}\left(\frac{l_m^{co} \sin\left(\alpha_m^o\right)}{l_m}\right) \tag{11}$$

Copyright © 2013 John Wiley & Sons, Ltd.

Prepared using cnmauth.cls
DOI: 10.1002/cnm

where α_m^o is the muscle pennation angle at optimal muscle fibre length, and l_m^{co} is the current optimal muscle fibre length given by:

$$l_m^{co} = l_m^o \left[\lambda(1 - a_m) + 1\right] \tag{12}$$

By including activation dynamics, the final governing relations consist of the coupled first-order and second-order differential Equations 9 and 5, *i.e.*

$$\frac{\partial^2 l}{\partial t^2} = \frac{F_t - F_m^{eff}}{M_m}$$

$$\frac{\partial a_m}{\partial t} = \frac{1}{\tau}\left(u_m - a_m\right)$$

where F_t is a function of l, and F_m^{eff} is a function of l, $\partial l/\partial t$ and a_m. The above system of equations is discretised using the implicit Euler method and solved by Newton's method for coupled system of nonlinear equations, as detailed in Appendix A. As a result, the current values of the three state variables, l, $\partial l/\partial t$ and a_m, are obtained. Hence, the current musculotendon force, as the main parameter of traction-based muscle boundary condition, can be determined.

Musculotendon Force

The musculotendon force F_{mt} is equal to the tendon force F_t given by Equation 7, which can be calculated using the current tendon length l_t:

$$l_t = l_{mt} - l_m \tag{14}$$

where l_{mt} is the musculotendon length and l_m is the muscle length. The musculotendon length, l_{mt}, is defined as the distance between the centroid of the insertion attachment boundary and the centroid of the origin attachment boundary, determined as:

$$l_{mt} = |\boldsymbol{C}_O - \boldsymbol{C}_I| \tag{15}$$

where $\boldsymbol{C}_O$ and $\boldsymbol{C}_I$ are the area weighted centroids of the musculotendon origin and insertion attachment surface meshes respectively, computed by:

$$\boldsymbol{C} = \sum_{i=1}^{N} \omega_i |\boldsymbol{\Gamma}_i| \tag{16a}$$

$$\omega_i = \frac{|\boldsymbol{\Gamma}_i|}{\sum_{j=1}^{N} |\boldsymbol{\Gamma}_j|} \tag{16b}$$

where $\boldsymbol{\Gamma}_i$ is the area vector of face i, N is the total number of faces on the attachment surface mesh, and ω_i are the face weights.

2.2. Muscle Mapping Procedure

Two separate musculotendon attachment approaches are considered here: the standard *point load* approach which assumes that the entire musculotendon force acts through an individual surface

Copyright © 2013 John Wiley & Sons, Ltd.

Prepared using cnmauth.cls
DOI: 10.1002/cnm

mesh node [36, 37], and in an attempt to realistically approximate the physiological mapping of muscle fibres, a *mapped* fibre procedure is developed.

The *mapped* approach transforms (maps) each muscle attachment surface mesh to a unit circle, calculating 2-D polar coordinates for each face centre on the attachment boundaries. It is then possible, for each face centre, to find the closest corresponding face centre on the other attachment site within 2-D polar space, as illustrated schematically in Figure 4.

To calculate the polar coordinates, R and θ, for each face centre $\boldsymbol{F}$ on the attachment boundaries, the positional vectors are defined as shown in Figure 5. The vector $\overrightarrow{\boldsymbol{CF}}$ connects the attachment boundary centroid $\boldsymbol{C}$ to the face centre of interest $\boldsymbol{F}$, where the calculation of $\boldsymbol{C}$ is given previously by Equation 16a. The vector $\overrightarrow{\boldsymbol{CF}}$ is extended to the attachment surface edge and the nearest boundary edge vertex $\boldsymbol{B}$ is found. The distance along the surface boundary edge from a reference vertex $\boldsymbol{O}$ to vertex $\boldsymbol{B}$ is designated as L, and the total attachment surface circumference is given as L_{total}.

The R coordinate of face centre $\boldsymbol{F}$ is then given by:

$$R = \frac{|\overrightarrow{\boldsymbol{CF}}|}{|\overrightarrow{\boldsymbol{CB}}|} \tag{17}$$

where $0 \leq R \leq 1$. The θ coordinate of face centre $\boldsymbol{F}$ is given by:

$$\theta = \frac{L}{L_{total}} \tag{18}$$

where $0 \leq \theta \leq 1$. Note that the θ coordinate is not necessarily related to the geometric angle.

A feature of the mapping procedure is that through appropriate placement of reference position $\boldsymbol{O}$ on each attachment, muscles with twisting fibres may be realistically approximated. Figure 6 shows a test case with circular attachment surfaces, where two separate locations of $\boldsymbol{O}$ are investigated showing how fibre twisting may be realistically represented. The position of reference position $\boldsymbol{O}$ is specified by the user at the beginning of the simulation, such that physiological fibre twisting may be captured.

Depending on the volume meshing strategy, it may be difficult or impossible to conform to the realistic muscle attachment sites during volume meshing. Accordingly, the current mapped fibre approach has been developed to employ surface mesh representations of the muscle attachment sites, which are independent of the volume mesh. The calculated muscle fibre directions are then interpolated to the surface of the actual volume mesh using an inverse-distance weighting procedure.

As boundary conditions to the continuum model, the muscle attachment traction field $\boldsymbol{T}_{mt}$ are calculated as:

$$\boldsymbol{T}_{mt} = \frac{F_{mt}}{S_{total}} \boldsymbol{d}_{mt} \tag{19}$$

where F_{mt} is the musculotendon force from the Hill-type model and $\boldsymbol{d}_{mt}$ are the musculotendon fibre directions determined by the *point load* or *mapping* procedures. The traction magnitudes are equal across each attachment site, the only difference being the traction directions.

In reality, the muscle fibres map in a bijective *one-to-one* manner from origin to insertion. However, as the current procedure assume that all fibres terminate at mesh face centres, this results in a surjective mapping when the origin and insertion surface meshes have unequal face numbers.

Copyright © 2013 John Wiley & Sons, Ltd.

Prepared using cnmauth.cls
DOI: 10.1002/cnm

Nonetheless, this effect is negligible when practical surfaces meshes, containing relatively high numbers of faces, are employed.

2.3. Geometry Generation & Meshing

Patient-specific hip geometry has been extracted from CT and MRI datasets of a 23-year-old male subject with no congenital or acquired pathology, employing the same subject as the gait analysis. As the procedure has been described previously [28–30], only a brief overview is given here. The CT images (512×512 pixels, $0.7422 \times 0.7422 \times 1.2500$ mm) and MRI images (256×256 pixels, $1.6797 \times 1.6797 \times 2.9999$ mm) spanning from mid femur to second lumbar vertebra were obtained using the GE medical systems LightSpeed VCT [38] and GE medical systems Signa HDxt [38] scanners, respectively. The bone surfaces have been segmented using open-source software 3DSlicer (version 4.0) [39], and have been smoothed, decimated and cleaned using open-source software Meshlab [40–42]. The final surfaces are exported in the STL format - a facet based surface composed of triangles.

The bone volumes are meshed in commercial software ANSYS ICEM CFD [43] using the surface independent Delaunay tetrahedral approach with prism boundary layers, where special attention is paid to partitioning the boundary surfaces into regions of interest - distal femur, femur head, acetabulum, iliosacral joint and pubic symphysis joint - for application of boundary conditions. Articular cartilage volume meshes are created by extruding the articular surfaces in the surface normal direction [12] by 0.6 mm, using the OpenFOAM utility `extrudeMesh`. The final high resolution hip joint volume mesh, containing a total of 569 418 cells (266 817 cortical, 253 316 cancellous, 49 285 cartilage), is shown in Figure 7.

Muscle Attachment Identification Using a manual segmentation procedure, the muscle attachment sites are extracted directly from CT and MRI datasets, which have been registered using a rigid transform based on mutual information [39], ensuring that both CT and MRI bone sets are coincident. The muscle attachment sites are then manually identified with reference to anatomical textbooks [44,45]. The procedure consists of selecting pixels along the muscle attachment site and pixels perpendicular to the bone surface inside and outside of the bone volume. This creates a pixel *bubble* encapsulating the muscle attachment, as shown in Figure 8. Intersection of this pixel *bubble* with the bone surface mesh allows generation of surface meshes of the realistic muscle attachments, which are employed in the *mapped* muscle fibre procedure.

2.4. Finite Volume Structural Solver

A FV-based structural contact solver, `elasticNonLinULSolidFoam`, has been specifically developed (in OpenFOAM software) to analyse the hip joint [29, 30, 46, 47]. Here, linear elastic material properties are assumed and the updated Lagrangian mathematical model is applied. Special attention is given to the contact algorithm, where a recently developed FV procedure based on the frictionless penalty method has been used [46]. Additionally, the solver is upgraded with the muscle boundary condition.

Copyright © 2013 John Wiley & Sons, Ltd.

Prepared using cnmauth.cls
DOI: 10.1002/cnm

Muscle Boundary Condition Parameters There are a number of muscle inputs required from the user at the beginning of the simulation. For each muscle, the five Hill-type parameters (F_{max}, l_m^o, α_m^o, l_t^s, M_m), the discrete time-varying muscle excitation signal u_m, and the muscle mapping method (*point load* or *mapped*) are provided. If the *point load* method is chosen, approximate insertion and origin attachment points must be supplied, where the procedure automatically selects the closest computational surface nodes. If the *mapped* method is chosen, a surface representation of each attachment site must be provided. Generation of these stereolithography (STL) attachment site surfaces is described in the previous section. Additionally, the coordinates of the insertion and origin reference positions must be specified ($\boldsymbol{O}_{\text{origin}}$ and $\boldsymbol{O}_{\text{insertion}}$), where the procedure selects the closest attachment boundary vertices.

Solver algorithm The solution procedure for this OpenFOAM solver may be summarised by the following steps:

(i) Read mesh, contact and muscle inputs;
(ii) Start time loop - iterate through all time increments;
(iii) Outer solution loop - iterate until momentum convergence;
(iv) Solve Hill-type models and update muscle boundary conditions;
(v) Update the contact between specified contact boundaries;
(vi) Solve momentum equation;
(vii) End solution loop;
(viii) Output results.
(ix) End time loop;

When the Hill-type models are solved, the current musculotendon length l_{mt}, calculated from the current mesh configuration, and the current excitation value, interpolated from the discrete excitation signal, are taken as inputs. If the time increments are relatively small, then the Hill-type muscle models need not be solved every outer iteration and may be corrected once per time increment. Steps (iii) through (vii) are repeated until the momentum system has converged.

2.5. Hip Joint Model Setup

The hip joint is numerically analysed at the *mid-stance* phase of the gait cycle where the relative positioning of the femur and pelvis is determined from gait analysis [29,30], and the effect of muscle attachment approach is investigated. All materials are represented as hypoelastic, homogenous and isotropic and the employed mechanical properties, previously displayed in Figure 7, are summarised in Table II.

In addition to the contact and muscle boundary conditions, the pelvis is fixed at the iliosacral and pubic symphysis joints (Figure 9), and the distal femur is displaced in the femur axial direction into the acetabulum such that resulting total hip joint force is equivalent to twice body weight (1 611 N), as measured *in vivo* by Bergmann et al. [48]. The remaining femur and pelvis surfaces are specified as traction-free and custom boundary conditions with non-orthogonal corrections are employed [30, 47]. The models are solved in one load increment where inertia and gravity forces are neglected.

Copyright © 2013 John Wiley & Sons, Ltd.

Prepared using cnmauth.cls
DOI: 10.1002/cnm

For the contact procedure, the pelvis articular cartilage surface is designated as the master and the femur articular surface as the slave. The contact penetration distances have been calculated using the *contact-spheres* approach [49]. A contact gap tolerance of 9×10^{-6} m is employed, the penalty factor is 6×10^{8} and the contact correction frequency is 40.

Although over 17 muscles may be considered to cause movement of the hip joint [44,50,51], only the abductors - *gluteus medius* and *gluteus minimus* - are considered here to illustrate the effects of the developed muscle mapping procedure. The numerical muscle fibre distributions for the *point load* and developed *mapped* approaches are compared in Figure 10. The employed Hill-type muscle parameters are presented in Table III. The first four muscle properties have been estimated from literature [19, 20, 24, 35, 36, 52–55], whereas muscle mass has been approximated by multiplying the muscle volume, calculated from tomography images, by the density of muscle tissue [21]. The reference positions for the mapped procedure are chosen such that the muscle fibres show negligible twisting.

3. RESULTS

As the current models are assumed steady-state, the muscle excitation values u_m corresponding to the *mid-stance* phase of gait are taken as the muscle model input values. The employed excitation values, determined from the processed EMG signals, are 0.196 for both the *gluteus medius* and *gluteus minimus* muscles. The total muscle forces predicted by the Hill-type muscle boundary conditions for each model are 317 N (active 142 N, passive 175 N) for *gluteus medius* and 270 N (active 19 N, passive 251 N) for *gluteus minimus*.

Comparing the computed numerical fibres with their anatomical counterpart, as shown in Figure 11, a qualitatively close agreement may be observed. The reason for differences is in the model approximation, where a musculotendon fibre is represented uniquely by a force vector, whereas in reality muscle and tendon are separate volumes.

Inspecting the predicted von Mises stress distributions, shown in Figure 12, appreciable differences can be seen between muscle attachment approaches. For the *point load* model, the attachment points of the muscles show local stress peaks of greater than 30 MPa predicted, whereas no local stress peaks are visible in the *mapped* attachments model. The greater trochanter, which is relatively unstressed in the model without muscles, bears considerably more load in models with muscles and supports higher stresses. Apart from the attachment stress peaks, in all the models the most highly stressed areas, of 30 to 50 MPa, are found in the ilium directly above the acetabulum, the acetabular roof bone as well as near the fixed iliosacral joint.

The predicted contact pressure distribution for the *point load* and *mapped* attachment models are shown side-by-side in Figure 13. The predicted maximum contact pressure, contact area and average contact pressure are summarised for all models in Table IV. Three distinct regions of contact are visible in each of the models, occurring in the same locations, and only slight differences are discernible.

Copyright © 2013 John Wiley & Sons, Ltd.

Prepared using cnmauth.cls
DOI: 10.1002/cnm

4. DISCUSSION

Comparing the *point load* and *mapped* models, there are notable differences in the stress distributions (Figure 12). The *point load* attachments result in local stress peaks of greater than 30 MPa, as has been previously noted in literature [36,37,55,56]. The magnitude of this stress peak is expected to increase with mesh refinement due to the load being applied to a single node [36,55]. The newly developed *mapped* muscle boundary conditions have been shown to overcome this problem of local erroneous stress peaks (Figure 12c). Additionally, when the computed numerical fibres are compared with their anatomical counterpart (Figure 11), good agreement has been found.

Apart from the local peaks, the stress distributions between the different muscle fibre approaches show differences in a number of regions, in particular in the neck of the femur highlighted in Figure 14. This suggests that the overall mechanics of the bone are different when more realistic *mapped* muscle attachments are employed.

Comparing the stress distributions of the models with muscles and the model without muscles, as expected there are significant differences in stress magnitudes in the vicinity of the muscle attachments. The greater trochanter, which is relatively unstressed in the model without muscles, carries relatively large stresses in the models with muscles. This is due to the convergence of the large abductor muscles to a comparatively small muscle attachment. Inspecting the pelvis, the body of the ilium also experiences a substantial increase in stress when muscles are included. The highly stressed regions of bone on the superior acetabular rim, remain largely unaffected by the inclusion of muscle models.

On closer analysis of the muscle forces predicted by the Hill-type muscle models, the predicted abductors force produced 0.73 times body weight, lying within the range of predictions in literature [2,3,57], where a variety of optimisation techniques are employed with inverse analysis.

The largest stresses in all of the models, occurring in the acetabular roof, the ilium above the acetabulum, the fixed iliosacral joint and the neck of the femur, agree well with predictions from previous numerical studies [4, 6, 16, 58–62]. The predicted maximum contact pressures are slightly larger than the reported values, where peak contact pressures in literature vary from 1 to 18 MPa [4,6,16,58–62], whereas the maximum predicted contact maximum pressures in the current models were 23–26 MPa. This is possibly explained by the combined effect of assuming joint congruency and using relatively low resolution meshes, common in literature, which may result in underestimation of contact pressures. Additionally, the current assumptions of constant cartilage thickness and homogenous mechanical properties may cause an overestimation of contact pressure.

Inspecting the contact pressure distributions, relatively subtle differences, if any, are seen between the muscle attachment approaches. Moreover, only minor differences are visible relative to the model without muscles, with two distinct contact regions predicted in all three models (Figure 13). Additionally, the predictions of contact area, average contact pressure and maximum contact pressure are very similar.

There are a number of limitations of the current approach, which should be stated: muscle wrapping is not represented; activation is assumed to be uniform across the entire muscle; only two distinct muscles are included and deep muscles are not included; the sensitivity to the muscle model parameters has not be investigated; multiple loading cases have not been examined; dynamic muscle parameters have been included although only a static analysis has been performed; and

Copyright © 2013 John Wiley & Sons, Ltd.

Prepared using cnmauth.cls
DOI: 10.1002/cnm

homogeneous trabecular bone stiffness has been assumed. Additionally, further validation of the model against experimental methods is important to provide confidence in the predictions, especially in the context of potential clinical applications, such as aiding in the design and development of next generation joint replacements, and contributing to the understanding of the mechanical causes of joint degeneration.

From the results of this study it is concluded that physiological joint loading is not accurately represented by simplistic peri-articular muscle approximations; however, when contact mechanics are of sole interest, then simplifying assumptions with regard to muscular forces may be valid.

ACKNOWLEDGEMENTS

Financial support from TEKNO Surgical Ltd. is gratefully acknowledged. The authors thank Mike Walsh and Damien Kiernan of the Central Remedial Clinic Dublin for conducting the gait analysis.

A. NUMERICAL SOLUTION OF HILL-TYPE GOVERNING RELATIONS

The governing system of the second-order and the first-order differential equations can be written as a system of three first-order differential equations in terms of state variables y_i $(i = 1, 2, 3)$:

$$\frac{\partial y_2}{\partial t} = \frac{F_t(y_1) - F_m^{eff}(y_1, y_2)}{M_m} \tag{A.1a}$$

$$\frac{\partial y_1}{\partial t} = y_2 \tag{A.1b}$$

$$\frac{\partial y_3}{\partial t} = \frac{1}{\tau}\left(u_m - y_3\right) \tag{A.1c}$$

where y_1, y_2 and y_3, are relative muscle position (l), muscle velocity ($\partial l/\partial t$) and muscle activation (a_m), respectively.

By employing the implicit Euler method on each first-order differential equation, the following discretised form can be obtained:

$$\frac{y_2^{i+1} - y_2^i}{h} = \frac{F_t(y_1^{i+1}) - F_m^{eff}(y_1^{i+1}, y_2^{i+1})}{M_m} \tag{A.2a}$$

$$\frac{y_1^{i+1} - y_1^i}{h} = y_2^{i+1} \tag{A.2b}$$

$$\frac{y_3^{i+1} - y_3^i}{h} = \frac{1}{\tau}\left(u_m - y_3^{i+1}\right) \tag{A.2c}$$

where h is the current time step and superscripts $(i + 1)$ and i refer to the current and previous time step values respectively.

Let us now define functions F, G and H as:

$$F = y_2^{i+1} - y_2^i - h\frac{F_t(y_1^{i+1}) - F_m^{eff}(y_1^{i+1}, y_2^{i+1})}{M_m} = 0 \tag{A.3a}$$

$$G = y_1^{i+1} - y_1^i - h y_2^{i+1} = 0 \tag{A.3b}$$

$$H = y_3^{i+1} - y_3^i - h\left[\frac{1}{\tau}\left(u_m - y_3^{i+1}\right)\right] = 0 \tag{A.3c}$$

Copyright © 2013 John Wiley & Sons, Ltd.

Prepared using cnmauth.cls
DOI: 10.1002/cnm

This discretised system of coupled nonlinear equations, A.3, may be solved using Newton's method for coupled systems of nonlinear equations [63–65], allowing construction of the linear system of equations:

$$\begin{aligned}
\frac{\partial F}{\partial y_1^i}\delta_1 + \frac{\partial F}{\partial y_2^i}\delta_2 + \frac{\partial F}{\partial y_3^i}\delta_3 &= -F \\
\frac{\partial G}{\partial y_1^i}\delta_1 + \frac{\partial G}{\partial y_2^i}\delta_2 + \frac{\partial G}{\partial y_3^i}\delta_3 &= -G \\
\frac{\partial H}{\partial y_1^i}\delta_1 + \frac{\partial H}{\partial y_2^i}\delta_2 + \frac{\partial H}{\partial y_3^i}\delta_3 &= -H
\end{aligned} \tag{A.4}$$

where the δ_i $(i = 1, 2, 3)$ terms are the unknown increments of the state variables y_i, and the partial derivate terms are calculated numerically using the finite difference method. This linear system can then be solved for δ_i using, for example, Gaussian elimination [64].

The current state variables are then updated using the newly found δ:

$$\begin{aligned}
y_1^{i+1} &= y_1^i + \delta_1 \\
y_2^{i+1} &= y_2^i + \delta_2 \\
y_3^{i+1} &= y_3^i + \delta_3
\end{aligned} \tag{A.5}$$

The linear system, A.4, is repeatedly solved and the state variables updated via A.5 until the system has converged to the predefined tolerance.

REFERENCES

1. Brekelmans WAM, Poort HW, Slooff TJJH. A New Method to Analyse the Mechanical Behaviour of Skeletal Parts. *Acta Orthopaedica* 1972; **43**(5):301–317.
2. Goel VK, Valliappan S, Svensson NL. Stresses in the normal pelvis. *Computers in Biology and Medicine* 1978; **8**:91–104.
3. Oonishi H, Isha H, Hasegawa T. Mechanical analysis of the human pelvis and its application to the artificial hip joint–by means of the three dimensional finite element method. *Journal of Biomechanics* 1983; **16**:427–44.
4. Dalstra M, Huiskes R, van Erning L. Development and validation of a three-dimensional finite element model of the pelvic bone. *Journal of Biomechanical Engineering* 1995; **117**:272–8.
5. Anderson AE, Peters CL, Tuttle BD, Weiss JA. Subject-specific finite element model of the pelvis: Development, validation and sensitivity studies. *Journal of Biomechanical Engineering* 2005; **127**:364–373.
6. Anderson AE. Computational modeling of hip joint mechanics. PhD Thesis, The University of Utah 2007.
7. Bachtar F, Chen X, Hisada T. Finite element contact analysis of the hip joint. *Medical & Biological Engineering & Computing* 2006; **44**:643–51.
8. Majumder S, Roychowdhury A, Pal S. Variations of stress in pelvic bone during normal walking, considering all active muscles. *Trends in Biomaterials and Artificial Organs* 2004; **17**(2):48–53.
9. Silvestri C. Development and validation of a knee-thigh-hip LS-Dyna model of a 50th precentile male. PhD Thesis, Worcester Polytechnic Institute 2008.
10. Anderson AE, Ellis BJ, Maas SA, Peters CL, Weiss JA. Validation of finite element predictions of cartilage contact pressure in the human hip joint. *Journal of Biomechanical Engineering* 2008; **130**:051 008.
11. Anderson AE, Ellis BJ, Peters CL, Weiss JA. Cartilage thickness: factors influencing multidetector ct measurements in a phantom study. *Radiology* 2008; **246**(1):133–141.
12. Anderson AE, Ellis BJ, Maas SA, Weiss JA. Effects of idealized joint geometry on finite element predictions of cartilage contact stresses in the hip. *Journal of Biomechanics* 2010; **43**:1351–7.

Copyright © 2013 John Wiley & Sons, Ltd.

Prepared using cnmauth.cls
DOI: 10.1002/cnm

13. Taylor M, Bryan R, Galloway F. Accounting for patient variability in finite element analysis of the intact and implanted hip and knee: A review. *International Journal for Numerical Methods in Biomedical Engineering* 2013; **29**(2):273–292.
14. Puso MA, Laursen TA. A 3D contact smoothing method using Gregory patches. *International Journal for Numerical Methods in Engineering* 2002; **54**(8):1161–1194.
15. Majumder S, Roychowdhury A, Pal S. Dynamic response of the pelvis under side impact load a three-dimensional finite element approach. *International Journal of Crashworthiness* 2004; **9**(1):89–103.
16. Pustoc'h A, Cheze L. Normal and osteoarthritic hip joint mechanical behaviour: a comparison study. *Medical & Biological Engineering & Computing* 2009; **47**(4):375–83.
17. Silvestri C, Mongiardini M, Ray MH. Improvements and validation of an existing LS-DYNA model of the knee-thigh-hip of a 50^{th} percentile male including muscles and ligaments. *7th European LS-DYNA Conference*, 2009.
18. Silvestri C, Ray MH. Development of a finite element model of the knee-thigh-hip of a 50th percentile male including ligaments and muscles. *International Journal of Crashworthiness* 2009; **14**:215–229.
19. Zajac FE. Muscle and tendon: properties, models, scaling, and application to biomechanics and motor control. *Critical Reviews in Biomedical Engineering* 1989; **17**(4):359–411.
20. Winters JM. *Hill-based muscle models: a systems engineering perspective*. Springer-Verlag Berlin and Heidelberg GmbH & Co. K, 1990.
21. Buchanan TS, Lloyd DG, Manal KT, Besier TF. Neuromusculoskeletal modeling: Estimation of muscle forces and joint moments and movements from measurements of neural command. *Journal of Applied Biomechanics* 2004; **20**:367–395.
22. Huxley AF. Muscular contraction. *The Journal of Physiology* 1974; **243**(1):1–43.
23. Gordon AM, Huxley AF, Julian FJ. The variation in isometric tension with sarcomere length in vertebrate muscle fibres. *Journal of Physiology* 1966; **184**:170–192.
24. Anderson F, Guendelman E, Habib A, Hamner S, Holzbaur K, John C, Ku J, Liu M, Loan P, Reinbolt J, *et al*.. OpenSim, version 2.4.0 2009.
25. Boor CD. *A practical guide to splines*. Springer, 2001.
26. CodaMotion Ltd. `http://www.codamotion.com` 2011.
27. Central Remedial Clinic, Dublin, Ireland. Gait analysis at the gait lab. `http://www.crc.ie` 2011.
28. Cardiff P, Karač A, FitzPatrick D, Flavin R, Ivanković A. Development of a Hip Joint Model for Finite Volume Simulations. *Journal of Biomechanical Engineering*, Accepted, 2013.
29. Cardiff P, Karač A, Flavin R, FitzPatrick D, Ivanković A. Modelling the muscles for hip joint stress analysis using a finite volume methodology. *18^{th} Bioengineering In Ireland*, Belfast, Northern Ireland, 2012.
30. Cardiff P. Development of the Finite Volume Method for Hip Joint Stress Analysis. PhD Thesis, University College Dublin 2012.
31. Konrad P. *The ABC of EMG*. Noraxon EMG & Sensor Systems, 2005.
32. Whittle M. *Gait analysis: an introduction*. 4^{th} edn., Butterworth-Heinemann Medical, 2007.
33. MATLAB. The mathworks inc. `http://www.mathworks.com/products/matlab` 2000.
34. Robleto RA. An analysis of the musculotendon dynamics of hill-based models. PhD Thesis, Texas Tech University 1997.
35. Cheng EJ, Brown IE, Loeb GE. Virtual muscle: a computational approach to understanding the effects of muscle properties on motor control. *Journal of Neuroscience Methods* 2000; **101**(2):117–30.
36. Phillips ATM, Pankaj P, Howie CR, Usmani AS, Simpson AHRW. Finite element modelling of the pelvis: inclusion of muscular and ligamentous boundary conditions. *Medical Engineering & Physics* 2007; **29**(7):739–748.
37. Olivetti N. Development of a hills model of the human knee-thigh-hip region for frontal car crash simulations. Master's Thesis, Politecnico di Milano 2006.
38. GE Healthcare. `http://www.gehealthcare.com` 2012.
39. Pieper S, Lorensen B, Schroeder W, Kikinis R. The NA-MIC Kit: ITK, VTK, Pipelines, Grids and 3D Slicer as an Open Platform for the Medical Image Computing Community. *Proceedings of the 3^{rd} IEEE International Symposium on Biomedical Imaging: From Nano to Macro*, vol. 1, 2006; 698–701.
40. Meshlab. `http://meshlab.sourceforge.net` 2012.
41. Vollmer J, Mencl R, Muller H. Improved laplacian smoothing of noisy surface meshes. *Eurographics* 1999; **18**(3):131–138.
42. Campen M, Kobbelt L, Attene M. A practical guide to polygon mesh repairing. *Eurographics 33^{rd} Annual Conference of the European Association for Computer Graphics*, Cagliari, Sardinia, France, 2012.
43. ANSYS Inc. ICEM CFD 13.0 user manual. `http://www.ansys.com/Products/Other+Products/ANSYS+ICEM+CFD` 2011.
44. Moore K, Agur A. *Essential clinical anatomy*. 5^{th} edn., Lippincott Williams & Wilkins: Philadelphia, 2005.

Copyright © 2013 John Wiley & Sons, Ltd.
Prepared using cnmauth.cls

DOI: 10.1002/cnm

45. Hofer M. *CT teaching manual: a systematic approach to CT reading*. Thieme, 2007.
46. Cardiff P, Karač A, Ivanković A. Development of a finite volume contact solver based on the penalty method. *Computational Material Science* 2012; **64**:283 – 284.
47. Cardiff P, Karač A, Tuković Ž, Ivanković A. Development of a finite volume based structural solver for large rotation of non-orthogonal meshes. 7^{th} *OpenFOAM Workshop*, Darmstadt, Germany, 2012.
48. Bergmann G, Deuretzbacher G, Heller M, Graichen F, Rohlmann A, Strauss J, Duda GN. Hip contact forces and gait patterns from routine activities. *Journal of Biomechanics* 2001; **34**:859–71.
49. Jasak H, Weller H. Finite volume methodology for contact problems of linear elastic solids. *Proceedings of* 3^{rd} *International Conference of Croatian Society of Mechanics*, Cavtat/Dubrovnik, Crotatia, 2000; 253–260.
50. Netter FH, Hansen J, Lambert D. *Netter's clinical anatomy*. Icon Learning Systems, 2008.
51. Gray H. *Neuroanatomy*. 2^{nd} edn., Churchill Livingstone, 2000.
52. Yamaguchi G, Sawa A, Moran D, Fessler M, Winters J. *A survey of human musculotendon actuator parameters*. Springer-Verlag Berlin and Heidelberg GmbH & Co. K, 1990.
53. Friederich JA, Brand RA. Muscle fiber architecture in the human lower limb. *Journal of Biomechanics* 1990; **23**(1):91 – 95.
54. Wickiewicz TL, Roy RR, Powell PL, Edgerton VR. Muscle architecture of the human lower limb. *Clinical Orthopaedics and Related Research* 1983; **179**.
55. Phillips ATM. The femur as a musculo-skeletal construct: a free boundary condition modelling approach. *Medical engineering & physics* 2009; **31**(6):673–80.
56. Cilingir AC, Ucar V, Kazan R. Three-dimensional anatomic finite element modelling of hemi-arthroplasty of human hip joint. *Trends in Biomaterials and Artificial Organs* 2007; **21**:63–72.
57. Heller MO, Bergmann G, Deuretzbacher G, Durselen L, Pohl M, Claes L, Haas NP. Musculo-skeletal loading conditions at the hip during walking and stair climbing. *Journal of Biomechanics* 2001; **34**(7):883–93.
58. Dalstra M, Huiskes R, Odgaard A, Van Erning L. Mechanical and textural properties of pelvic trabecular bone. *Journal of Biomechanics* 1993; **26**(4-5):523–535.
59. Brown TD, DiGioia AM. A contact-coupled finite element analysis of the natural adult hip. *Journal of Biomechanics* 1984; **17**:437–48.
60. Hodge WA, Fijan RS, Carlson KL, Burgess RG, Harris WH, Mann RW. Contact pressures in the human hip joint measured in vivo. *Proceedings of the National Academy of Sciences of the United States of America* May 1986; **83**(9).
61. Russell ME, Shivanna KH, Grosland NM, Pedersen DR. Cartilage contact pressure elevations in dysplastic hips: a chronic overload model. *Journal of Orthopaedic Surgery and Research* 2006; **1**:6.
62. Harris MD, Anderson AE, Henak CR, Ellis BJ, Peters CL, Weiss JA. Finite element prediction of cartilage contact stresses in normal human hips. *Journal of Orthopaedic Research: Official Publication of the Orthopaedic Research Society* 2011; 1133–1139.
63. Kiusalaas J. *Numerical methods in engineering with MATLAB*. Cambridge University Press, 2005.
64. Hauser J. *Numerical Methods for Nonlinear Engineering Models*. Springer, 2009.
65. Higham N. *Accuracy and stability of numerical algorithms*. Society for Industrial and Applied Mathematics, 1996.
66. Pitman MI, Peterson L. *Basic biomechanics of the musculoskeletal system*, chap. Biomechanics of skeletal muscle. 2^{nd} edn., Lea & Febiger: Philadelphia, PA, 1989; 44–65. *eds* Nordin M. and Frankel V. H.
67. Teitz C, Graney D. A musculoskeletal atlas of the human body. Accessed online February 2013, `http://depts.washington.edu/msatlas` 2013.
68. Jonkers I, Sauwen N, Lenaerts G, Mulier M, Van Der Perre G, Jaecques S. Relation between subject-specific hip joint loading, stress distribution in the proximal femur and bone mineral density changes after total hip replacement. *Journal of Biomechanics* 2008; **41**:3405–13.
69. Taylor M, Tanner KE, Freeman MAR, Yettram AL. Cancellous bone stresses surrounding the femoral component of a hip prosthesis: an elastic-plastic finite element analysis. *Medical Engineering & Physics* 1995; **17**(7):544–550.
70. Mesfar W, Shirazi-Adl A. Biomechanics of the knee joint in flexion under various quadriceps forces. *The Knee* 2005; **12**:424–434.

Copyright © 2013 John Wiley & Sons, Ltd.
Prepared using cnmauth.cls

DOI: 10.1002/cnm

LIST OF FIGURES

Copyright © 2013 John Wiley & Sons, Ltd.
Prepared using cnmauth.cls

DOI: 10.1002/cnm

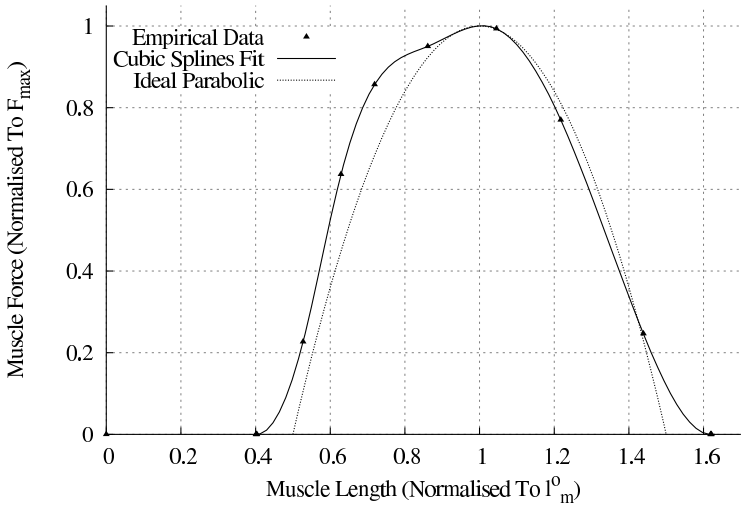

Figure 1. Muscle Force-Length Relationship

Copyright © 2013 John Wiley & Sons, Ltd.
Prepared using cnmauth.cls

DOI: 10.1002/cnm

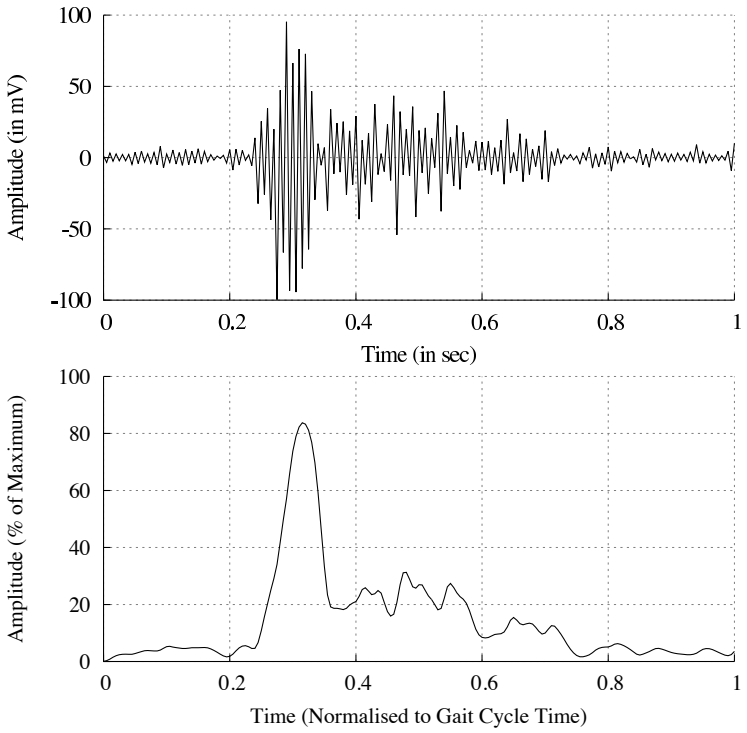

Figure 2. Processing of EMG Signals

Copyright © 2013 John Wiley & Sons, Ltd.
Prepared using cnmauth.cls

DOI: 10.1002/cnm

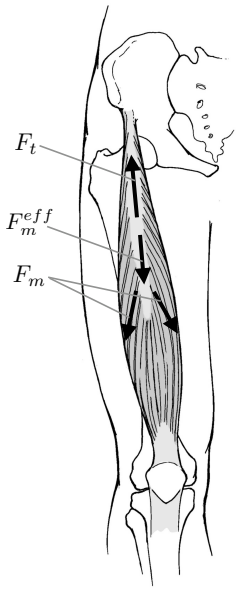

Figure 3. Effective Muscle Force due to Muscle Pennation Angle (Adapted from [66])

Copyright © 2013 John Wiley & Sons, Ltd.
Prepared using cnmauth.cls

DOI: 10.1002/cnm

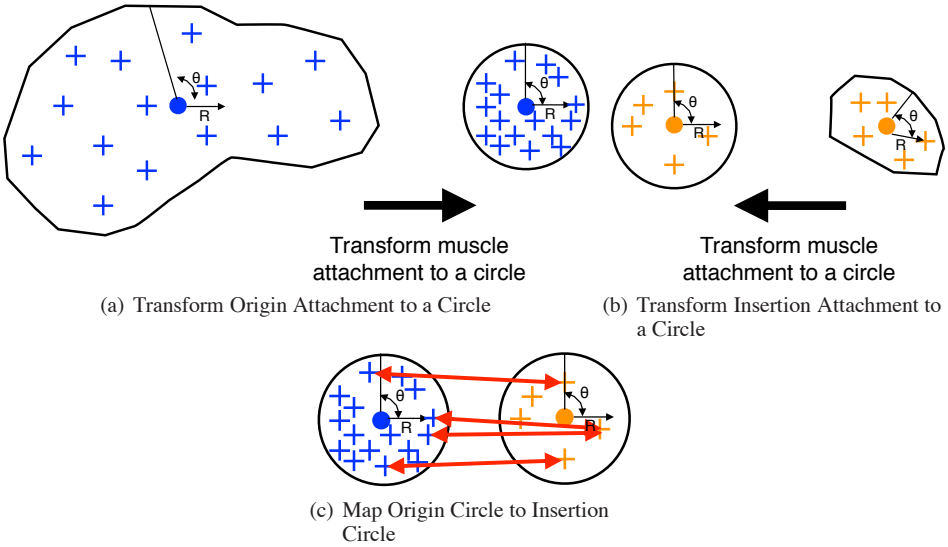

(a) Transform Origin Attachment to a Circle

(b) Transform Insertion Attachment to a Circle

(c) Map Origin Circle to Insertion Circle

Figure 4. Schematic of *Mapped* Fibre Direction Approach

Copyright © 2013 John Wiley & Sons, Ltd.
Prepared using cnmauth.cls

DOI: 10.1002/cnm

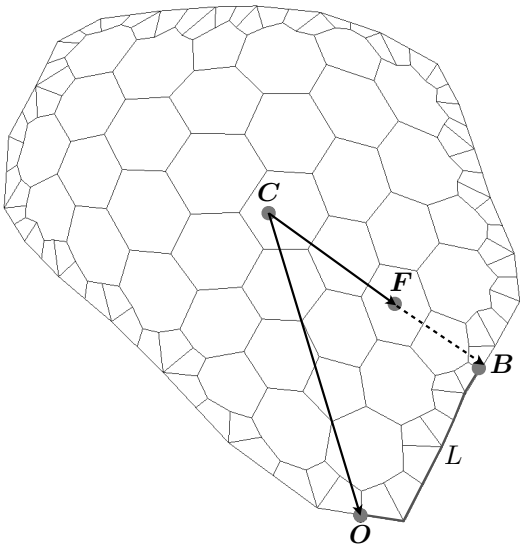

Figure 5. Calculation of the R Coordinate and θ Coordinate for Face Centre $\boldsymbol{F}$ on the Attachment Surface Mesh

Copyright © 2013 John Wiley & Sons, Ltd.
Prepared using cnmauth.cls

DOI: 10.1002/cnm

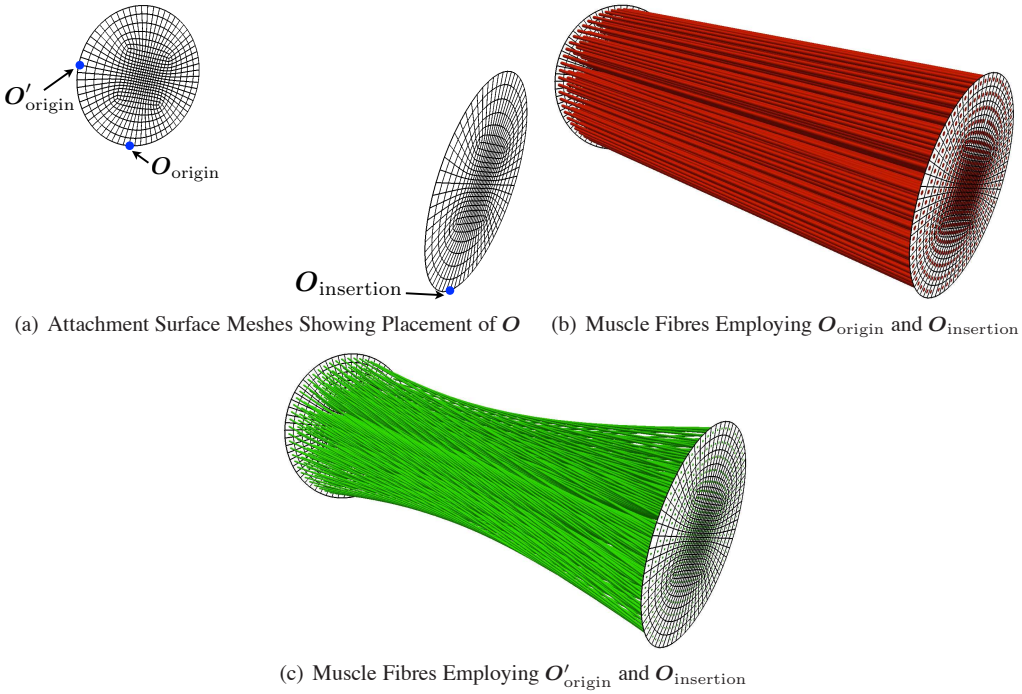

(a) Attachment Surface Meshes Showing Placement of O

(b) Muscle Fibres Employing O_{origin} and $O_{\text{insertion}}$

(c) Muscle Fibres Employing O'_{origin} and $O_{\text{insertion}}$

Figure 6. Effect of Reference Position O on Fibre Directions

Copyright © 2013 John Wiley & Sons, Ltd.
Prepared using cnmauth.cls

DOI: 10.1002/cnm

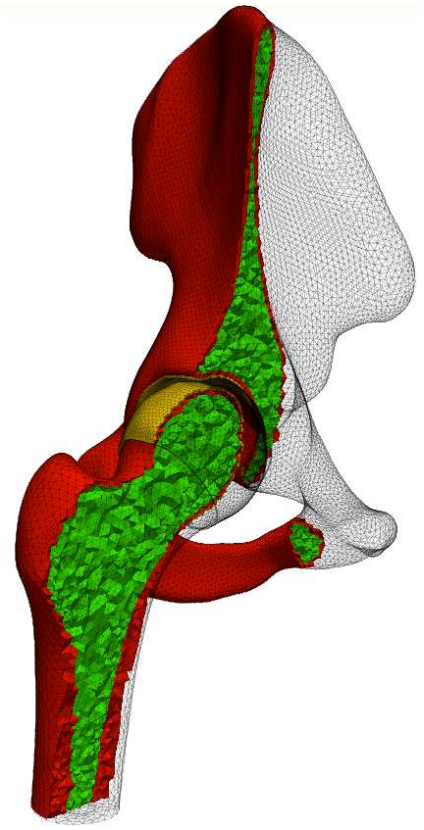

Figure 7. Hip Joint Model Material Distribution (Cortical Bone in Red, Cancellous Bone in Green and Cartilage in Yellow, Cells Removed for Visualisation)

Copyright © 2013 John Wiley & Sons, Ltd.
Prepared using cnmauth.cls

DOI: 10.1002/cnm

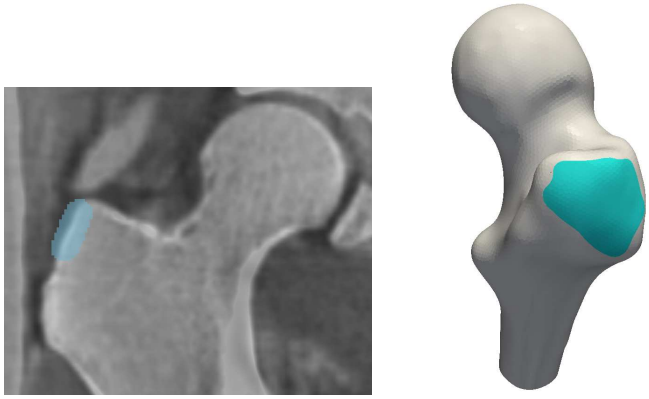

(a) Selection of Pixels (*Blue*)

(b) Identified Muscle Attachment

Figure 8. Segmentation of Muscle Attachment Sites Using Pixel *Bubbles*

Copyright © 2013 John Wiley & Sons, Ltd.
Prepared using cnmauth.cls

DOI: 10.1002/cnm

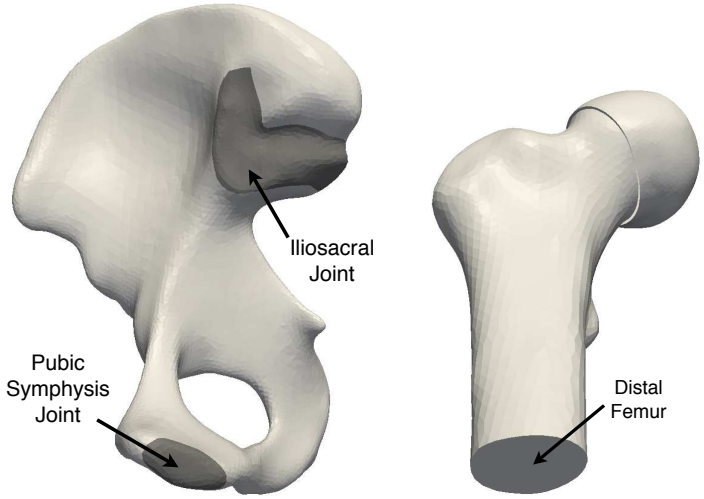

(a) Fixed Iliosacral & Pubic Symphysis Joints

(b) Displaced Distal Femur

Figure 9. Hip Joint Model Boundary Conditions

Copyright © 2013 John Wiley & Sons, Ltd.
Prepared using cnmauth.cls

DOI: 10.1002/cnm

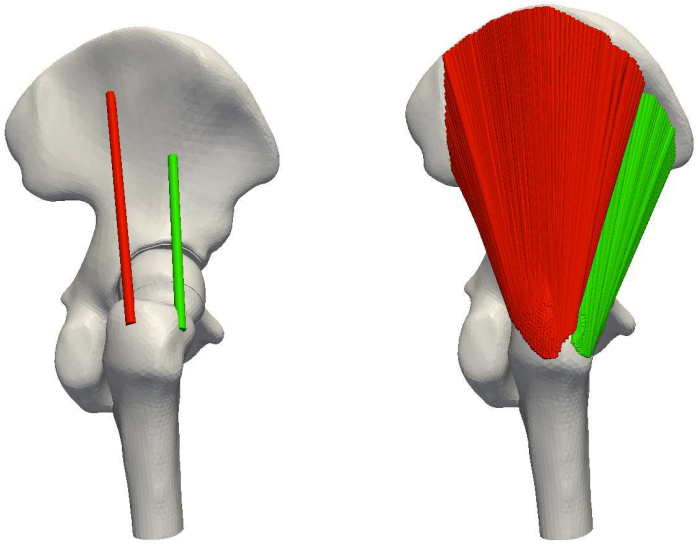

(a) Point Load Attachments (b) Mapped Attachments

Figure 10. Comparison of Muscle Attachment Approaches for the *Mid-Stance* Model (*Gluteus Medius* in Red, *Gluteus Minimus* in Green)

Copyright © 2013 John Wiley & Sons, Ltd.
Prepared using cnmauth.cls

DOI: 10.1002/cnm

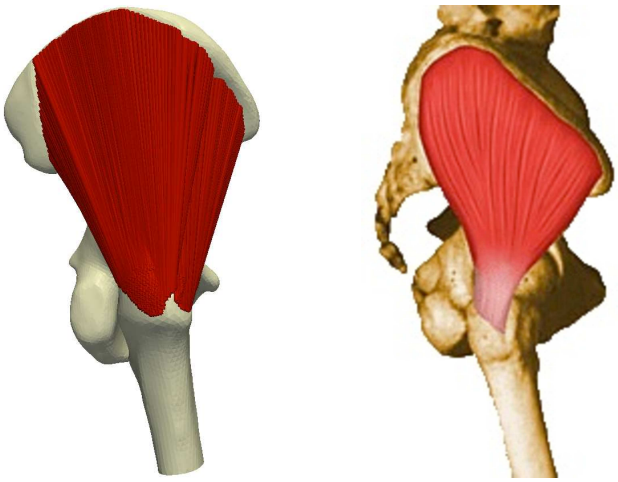

(a) *Mapped* (b) Anatomical [67]

Figure 11. Comparison of the *Mapped* Muscle Fibre Directions with the Anatomical Muscle

Copyright © 2013 John Wiley & Sons, Ltd.
Prepared using cnmauth.cls

DOI: 10.1002/cnm

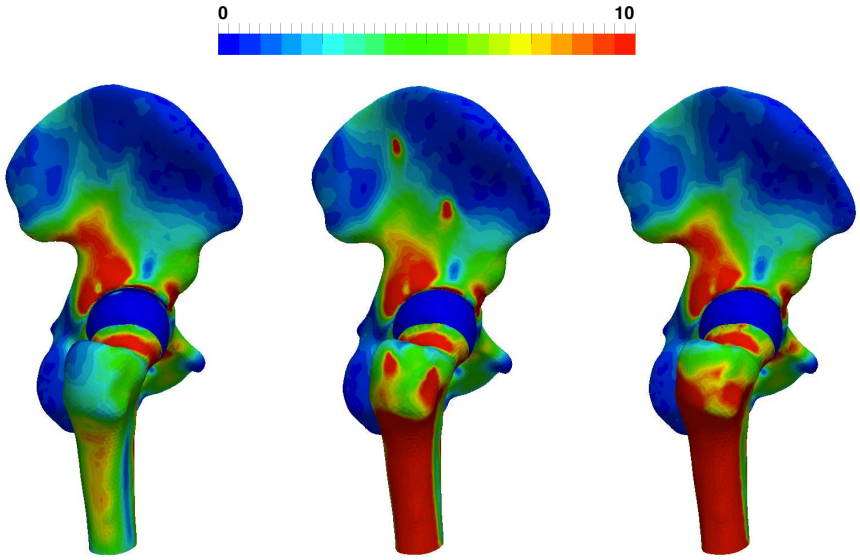

(a) No Muscles (b) *Point Load* (c) *Mapped*

Figure 12. Von Mises Stress Distribution Comparing Attachment Approaches (in MPa)

Copyright © 2013 John Wiley & Sons, Ltd.
Prepared using cnmauth.cls

DOI: 10.1002/cnm

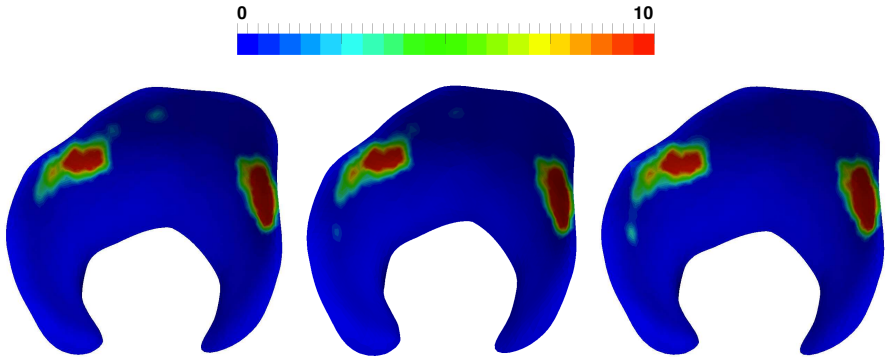

(a) No Muscles (b) *Point Load* (c) *Mapped*

Figure 13. Effect of Muscle Attachment Approach on the Contact Pressure Distribution (in MPa)

Copyright © 2013 John Wiley & Sons, Ltd.
Prepared using cnmauth.cls

DOI: 10.1002/cnm

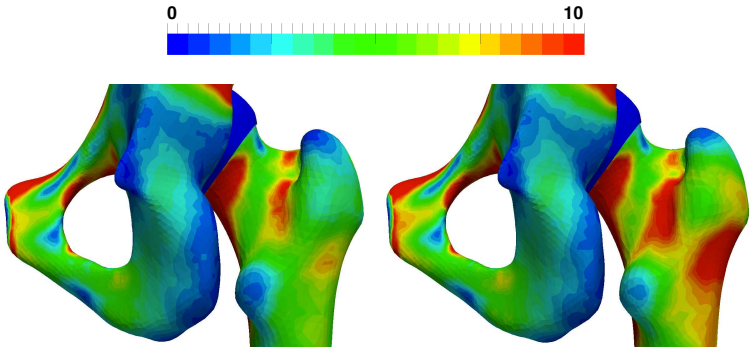

(a) *Point Load* (b) *Mapped*

Figure 14. Effect of Muscle Attachment Approach on the von Mises Stress Distribution (in MPa)

Copyright © 2013 John Wiley & Sons, Ltd.
Prepared using cnmauth.cls

DOI: 10.1002/cnm

LIST OF TABLES

Copyright © 2013 John Wiley & Sons, Ltd.
Prepared using cnmauth.cls

DOI: 10.1002/cnm

Parameter	a	$a^{'}$	b	$b^{'}$	F_{ecc}
Value	$0.25\,F_{max}$	$0.25\,F_{max}$	$0.25\,v_{max}$	$0.25\,v_{max}$	1.8

Table I. Force-Velocity Relationship Shape Parameters

Copyright © 2013 John Wiley & Sons, Ltd.
Prepared using cnmauth.cls

DOI: 10.1002/cnm

	Young's Modulus	Poisson's Ratio
Cortical Bone	17 GPa	0.3
Cancellous Bone	800 MPa	0.2
Cartilage	12 MPa	0.45

Table II. Mechanical Properties [2,4,7–9,12,16,58,61,62,68–70]

Copyright © 2013 John Wiley & Sons, Ltd.
Prepared using cnmauth.cls

DOI: 10.1002/cnm

Property	Gluteus Medius	Gluteus Minimus
F_{max}	1365 N	585 N
l_m^o	0.068 m	0.054 m
α_m^o	9 °	4 °
l_t^s	0.061 m	0.031 m
M_m	0.463 kg	0.232 kg

Table III. Hill-Type Muscle Model Parameters

Copyright © 2013 John Wiley & Sons, Ltd.
Prepared using cnmauth.cls

DOI: 10.1002/cnm

Model	Max Pressure (in MPa)	Contact Area (in m^2)	Average Pressure (in MPa)
No Muscles	26	3.96×10^{-4}	6.28
Point Load	24	4.05×10^{-4}	6.2
Mapped	23	4.01×10^{-4}	6.4

Table IV. Contact Predictions

Copyright © 2013 John Wiley & Sons, Ltd.
Prepared using cnmauth.cls

DOI: 10.1002/cnm